Interfacial Embedding of Laser-Manufactured Fluorinated Gold Clusters Enabling Stable Perovskite Solar Cells with Efficiency Over 24%

Pengfei Guo[1,8], Hongfu Zhu[2,3,8], Wenhao Zhao[1], Chen Liu[1], Liguo Zhu[3,4], Qian Ye[1], Ning Jia[1], Hongyue Wang[1], Xiuhai Zhang[1], Wanxia Huang[2], Vladimir A. Vinokurov[5], Evgenii Ivanov[5], Dmitry Shchukin[6], Jose María Ulloa[7], Adrian Hierro[7], and Hongqiang Wang[1*]

1. State Key Laboratory of Solidification Processing, Center for Nano Energy Materials, School of Materials Science and Engineering, Northwestern Polytechnical University and Shaanxi Joint Laboratory of Graphene (NPU), Xi'an, 710072, China

2. College of Materials Science and Engineering, Sichuan University, Chengdu, 610065, China

3. Institute of Fluid Physics, China Academy of Engineering Physics, Mianyang, 621900, China

4. Microsystem & Terahertz Research Center, China Academy of Engineering Physics, Chengdu, 610200, China

5. Gubkin Russian State University of Oil and Gas, Gubkin University, 19991, Moscow, 65/1 Leninsky prospect, Russia

6. Stephenson Institute for Renewable Energy, University of Liverpool, Liverpool L69 7ZF, UK

7. ISOM, Universidad Politécnica de Madrid, 28040 Madrid, Spain

8. These authors contributed equally: Pengfei Guo, Hongfu Zhu.

*Email: hongqiang.wang@nwpu.edu.cn

Abstract:

Tackling the interfacial loss in emerged perovskite-based solar cells (PSCs) to address synchronously the carrier dynamics and the environmental stability, has been of fundamental and viable importance, while technological hurdles remain in not only creating such interfacial mediator, but the subsequent interfacial embedding in the active layer. This article reports a strategy of interfacial embedding of hydrophobic fluorinated-gold-clusters (FGCs) for highly efficient and stable PSCs. The p-type semiconducting feature enables the FGC efficient interfacial mediator to improve the carrier dynamics by reducing the interfacial carrier transfer barrier and boosting the charge extraction at grain boundaries. The hydrophobic tails of the gold clusters and the hydrogen bonding between fluorine groups and perovskite favor the enhancement of environmental stability. Benefiting from these merits, highly efficient formamidinium lead iodide PSCs (champion efficiency up to 24.02%) with enhanced phase stability under varied relative humidity (RH) from 40% to 95%, as well as highly efficient mixed-cation PSCs with moisture stability (RH of 75%) over 10 000 h are achieved. It is thus inspiring to advance the development of highly efficient and stable PSCs via interfacial embedding laser-generated additives for improved charge transfer/extraction and environmental stability.

Key words: Perovskite solar cell; Interfacial loss; Pulsed laser irradiation; Gold clusters; Environmental stability

Introduction

The recent decades have witnessed the success of plannar opotoelectronics in photovoltaic[1], light-emitting[2], photodetecting[3], and photoelectrochemistry[4], while the electronic loss arising from the interfacial band alignment and carrier recombination has become the dominate factors of limiting the device performance. Addressing the interfacial loss is thus of paramount importance and particularly urgent in emerged perovskite solar cells, owing to the roles of interfacial engineering on modulating the interfacial carrier dynamics, as well as the environmental stability[5,6]. General engineering of a buffer layer at perovskite/charge-transport layer (CTL) interfaces has achieved great success in reducing the interfacial carrier recombination and/or charge extraction losses, owing to the modification of the physicochemical properties at the involved interfaces[7]. Considering the polycrystalline nature of perovskite films, grain boundaries (GBs) with abundant wrong or dangling bonds, which serve as centers of carrier recombination and energy barrier of charge transfer as well as first sites of perovskite decomposition, have also played an equivalently crucial role in ruling performance and stability of PSCs[8-13]. The recent success on decreasing trap densities and stabilizing perovskite based on the surface and GB co-passivation strategy[14,15], confirms that engineering at the GBs is even more important than that of surface-only. Addressing the interface loss at both perovskite surface and GBs has thus been of significance for pursuing highly efficient and stable PSCs[13].

The most dominate strategies of addressing the interfacial loss at surface and grain boundaries is molecular passivation. Preliminary successes have been demonstrated by dissolving molecular additives in perovskite precursor or through anti-solvent to reduce non-radiative recombination based on either coordination, or covalent bonding between the passivation molecules and perovskite[14,16-19]. However, obstacles of charge extraction/transfer will be generally encountered at GBs within the perovskite layer and/or at the interface between perovskite absorber and CTL due to the general insulation feature of the passivation molecules. By virtue of the advances in conductivity and functionality, inorganic nanocrystals such as carbon dots[20,21], black phosphorus[22], lead sulfide[23,24], and MXene[25],

have been demonstrated to provide more spaces on modulating interfacial carrier dynamics than those of molecular additives. A notable example is that engineering of the perovskite absorber and perovskite/CTL interfaces by employing ultrathin MXene enables the regulation of the work function of the perovskite layer and CTL, improves the electron/hole extraction efficiency, and consequently leads to the enhanced power conversion efficiency[26]. Despite the overwhelming advantages in the modulation of carrier dynamics, the long-term stability of PSCs that is critically required for commercialization based on the modification of inorganic nanocrystals lag much behind those of molecular additives, owing to the incapability of nanocrystals additives on restraining the perovskite from degradation by external environmental stimuli. It would thus be highly promising to advance the PSCs based photovoltaics through endowing the nanocrystals based additives with the important function of addressing the environmental stability of PSCs. Technological hurdles remain however in not only on creating such a bi-functional additive, but the subsequent interfacial embedding of them in the active layer.

This article presents an efficient strategy of interfacial engineering through embedding hydrophobic fluorinated gold clusters (FGCs) in the active layer for highly efficient and stable PSCs. Thanks to the universal and unique feature of pulsed laser irradiation in liquid for generating various nanocrystals in desired solvents, p-type semiconducting FGCs were generated in ethyl acetate (EA) and embedded at both surface and GBs of the perovskite film by following a simple anti-solvent procedure (**Fig. 1a**)[20,27]. The embedding of such FGCs can serve as a bifunctional interfacial mediator in PSCs (**Fig. 1b)** where the FGCs with intrinsic molecular-like behavior and resulted hydrophobicity facilitate the extraction/transfer both at GBs of perovskite active layer and at interface between perovskite and hole transport layer, as well as efficiently impeding the degradation of the vulnerable perovskite. This article details the recent achievement that by virtue of the bi-function of interfacial mediating, highly efficient mixed-cation PSCs with moisture durability over 10000 hours (75% RH), as well as FAPbI$_3$ PSCs

with champion PCE up to 24.02% and significantly enhanced environmental stability, which rank among the top records in PSCs decorated with nanocrystals based additives, is possible (**Supplementary Table S1**).

Results

Preparation of fluorinated-gold-clusters (FGCs). FGCs and their larger plasmonic counterpart are directly manufactured in an anti-solvent of ethyl acetate (EA) via the pulsed laser irradiation of the gold target. Briefly, bulk gold was placed in EA with or without the presence of 1H,1H,2H,2H-Perfluorodecanethiol (PFDT), and then subjected to irradiation by a non-focused pulsed laser beam with a wavelength of 355 nm and tunable laser fluence (Supplementary **Fig. 1**), consequently generating corresponding FGCs colloidal solution and its counterpart (gold nanocrystals, denoted as GNs). The formed colloidal solutions exhibited different color and ultraviolet-visible (UV-vis) absorption spectra (Supplementary **Fig. 2**), where the colloidal solution of GNs exhibited typical surface plasmon resonance (SPR) absorption originated from collective oscillation of electrons driven by visible light[28]. In contrast, the colloidal solution of FGCs demonstrated quenched SPR signal in the absorption spectra and apparent photoluminescence at 450 nm, which is similar with the unique molecular-like behavior of gold clusters that originates from its discrete electronic state induced by the quantum confinement effect[29,30].

Figure 1a shows transmission electron microscope (TEM) and high-resolution TEM (HRTEM) images of FGCs, respectively. The FGCs exhibit the monodispersity with an average size of 1.5 nm by counting over 200 units. Lattice fringes with an inner-plane spacing at 0.24 nm are depicted in inset in **Fig. 1a**, corresponding to the (111) facet of the face-centered cubic Au[31], which is consistent with the result of the fast Fourier transform (FFT) pattern. In comparison, the GNs exhibit broad size distribution and an average size of 8 nm (Supplementary **Fig. 3**), which indicates that the ligand of PFDT is crucial to obtain well dispersed gold clusters. X-ray photoelectron spectroscopy (XPS) was further employed to identify surface character of the FGCs (**Fig. 1b,c** and Supplementary **Fig. 4**). **Figure 1b** shows the high-resolution XPS spectrum of C 1s for the FGC, which could be fitted into peaks of C-C, C-S, -

CF$_2$ and -CF$_3$[15,32], indicating the grafting of the long fluorocarbon chain on the surface of the clusters. It can also be observed that the Au 4f spectrum (**Fig. 1c**) contains two main peaks at 84.2 (Au 4f 7/2) and 87.9 eV (Au 4f5/2) respectively, and the peak of Au 4f could be fitted to two states of Au(0) and Au(I)[31,33], latter of which indicate the interfacial covalent bridging between Au cluster and the ligand of PFDT, i.e. the formation of the Au-S bonding. With such covalent bonding, the colloidal solution of FGCs has outstanding stability upon aging for six months (Supplementary **Note 1**).

Interfacial embedding of FGCs into perovskite films. Following a typical anti-solvent procedure (Supplementary **Fig. 5**), we fabricated the mixed-cation perovskite films (Cs$_{0.05}$(FA$_{0.85}$MA$_{0.15}$)$_{0.95}$PbI$_{2.55}$Br$_{0.45}$, CsFAMA) on TiO$_2$/FTO substrates by embedding the as-prepared GNs and FGCs in the films of CsFAMA, respectively, and denoted them as 'CsFAMA/GNs' and 'CsFAMA/FGCs', while the film using EA-only as anti-solvent was denoted as 'control'. **Figure 1d** shows the top-view scanning electron microscopy (SEM) images of perovskite films. It can be observed that the embedding of FGCs in this study lead to no alteration of grain-size but the improvement of the surface smooth and the compactness compared to the films of control and CsFAMA-GNs (Supplementary **Fig. 6**), indicating that the FGCs could act as the bridge for crosslinking of the adjacent grains of perovskite. Introducing of FGCs also leads to better orientation of perovskite films along the direction perpendicular to the substrate, i.e. (001), as shown in the X-ray diffraction (XRD, Supplementary **Fig. 7**) patterns. The XRD analysis demonstrates no phase change and no shift of diffraction peaks, which indicates that the introducing of FGCs has no influence on the crystalline of perovskite, reflecting that the introduced FGCs locates possibly out of the perovskite grains.[14,20].

Cross-sectional TEM was employed to investigate the distribution of FGCs within the perovskite layer. As shown in **Fig. 1e**, the CsFAMA/FGCs film shows single-grain feature along the perpendicular direction of the perovskite layer that favors for fast carrier transport[34]. The FGCs were found uniformly distributed across the entire perovskite layer, as shown in **Fig. 1f**, which is different from the case of large-sized GNs (Supplementary **Fig. 8-9,**

preferentially locating at both of the surface and bottom in the perovskite layer). Cross-sectional HRTEM was further used to determine the specific location of FGCs, as shown in **Fig. 1g** and Supplementary **Fig. 10**, and confirmed that the FGCs are evenly embedded at the surface and GBs of perovskite film. The three selected regions along the grain boundaries shown in **Fig. 1g** clearly depicted the lattice fringes of FGC with an inner-plane spacing at 0.24 nm and the surrounded perovskite grains with the typical inner-plane spacing of 0.31 nm in (002) or 0.21nm in (220), which are further verified by the FFT analysis (insets of the **Fig. 1g**). The examination on lattice fringe and FFT patterns within the grain (Supplementary **Fig. 10**) was also carried out to exclude the existence of the FGCs in perovskite lattice. Such direct observation of the location of FGCs in the perovskite layer is in good agreement with the little phase change/peaks shift in the XRD analysis.

Photovoltaic performance and stability of FGCs embedded perovskite solar cells. PSC devices with the planar configuration of FTO/TiO$_2$/CsFAMA/Spiro-OMeTAD/Au (**Fig. 3a**) were constructed to investigate the roles of embedding FGCs at the surfaces and GBs of perovskite layer on the photovoltaic performance. The effect of the concentration of the FGC as well as the additive volume of PFDT were systematically studied (Supplementary **Figs. 11-14**, **Tables 2-2**, and **Note. 1**), and the optimized parameters of generating FGCs for enhanced performance of PSCs was determined as 1 vol% in the anti-solvent of EA with laser irradiation time of 5 min, which yielded FGCs colloidal solution with little residual of PFDT. Current density-voltage (*J-V*) curves of the PSCs were measured in reverse scan (RS) and forward scan (FS) under a simulated sunlight of air mass (AM) 1.5 G, as shown in **Fig. 3b** and **Table 1**. The control device achieves a champion PCE of 20.67% in RS, with a short circuit current density (J_{SC}) of 22.80 mA/cm^2, an open circuit voltage (V_{OC}) of 1.150 V, and a fill factor (FF) of 78.84%. The champion device embedded by FGCs yields a PCE of 21.90% with all improved photovoltaic parameters, much higher than that of GNs (champion efficiency of 21.36%). The integrated J_{SC} from external quantum efficiency (EQE) spectra matches well with the values measured from *J-V* curves for all the devices (<5% discrepancy, Supplementary **Fig.**

15). A negligible hysteresis (1.3%) is presented on the CsFAMA/FGCs device in comparison with those of control (10.5%) and CsFAMA/GNs (14.4%). As shown in **Fig. 3c**, the FGCs embedded device delivers a stabilized PCE of 21.60%, whereas the control and CsFAMA/GNs devices exhibit decreased PCEs of 18.84% and 18.96%, respectively. Additionally, the devices based on the construction of CsFAMA/FGCs exhibit better reproducibility compared with those of the control and CsFAMA/GNs (Supplementary **Fig. 16**). The average PCE for the CsFAMA/FGCs device rises from 19.66 % to 21.02 % with the improvement of V_{OC}, J_{SC} and FF, owing to the suppressed charge carrier recombination (Supplementary **Fig. 17**) as well as the enhanced EQE in long wavelength from 650 to 750 nm that is out of the typical SPR range of GNs (Supplementary **Fig. 15**)[35]. Comparatively, the average PCE for the CsFAMA/GNs device only increases to 20.02%, resulting from the trade-off between significantly increased J_{SC} and mildly decreased V_{OC}.

It is also worth noting that the FGCs adopted for embedding are hydrophobic because of the grafted long fluorocarbon chain[14,15]. The interfacial embedding of FGCs in the perovskite films is thus able to passivate the ingression pathway of water and improve their long-term moisture stability. The stability of CsFAMA devices exposed to different conditions was then evaluated. As shown in **Fig. 3d**, the PCE of the CsFAMA/GNs device is continuously decreased from pristine 20.07 ± 0.42% to 9.70 ± 1.45% after 60 days under the condition of 75% relative humidity (RH) at room temperature (RT), similar with trend of the control device (Supplementary **Fig. 18**), whereas the CsFAMA/FGCs device still maintains over 95% (19.82 ± 0.59%) of its initial efficiency (20.75 ± 0.41%) after aging over 10000 hours. The operational stability of CsFAMA devices was tracked over time at the maximal power point (MPP) aged under continuous light (100 mW/cm^2) in an inert atmosphere (**Fig. 3e**). The control device with an initial PCE of 20.07% degrades continuously to 70% in 125 hours. Similar to the control device, the CsFAMA/GNs device presents a same decrease trend in 200 hours, where the initial PCE of 20.83% gradually

decreases to 14.91%. Comparatively, the CsFAMA/FGCs device impressively undergoes a plateau during long-time aging of 500 hours after a slow decrease in the first 50 hours, and maintains >90% of its initial efficiency (21.02%).

Further thermal stability testing of the PSCs was conducted at elevated temperature in an inert environment (Supplementary **Fig. 19**), where the CsFAMA/GNs devices show a continuous decay in PCE, and even faster decrease than control ones, with the temperature increasing from 75 °C to 100 °C after 50 hours, owing to the decomposition of the perovskite film induced by the interaction between perovskite and Au as well as the migration of Au[36]. Surprisingly, the CsFAMA/FGCs devices still maintain their initial PCE. Further long-term thermal stability tracking at 85°C for the CsFAMA/FGCs and CsFAMA/GNs devices is shown in **Fig. 3f**. The CsFAMA/GNs device degrades by more than 44% in 1000 hours, whereas the CsFAMA/FGCs device maintains >92% (18.98 ± 0.46%) of its initial efficiency (20.51 ± 0.13%). This reflects the important roles of grafting of PFDT on gold cluster via formation of Au-S covalent bonding. In addition, the stability test was performed in a temperature-variable environment from RT to 10K and back again to RT, via tracking the *I-V* curves by focusing a modulatory-monochromatic beam of light onto the perovskite devices (Supplementary **Fig. 20**). As shown in **Fig. 3g**, the CsFAMA/FGCs device delivers a higher photo-generated current than that of the control, regardless of the temperature being at RT or 10K, demonstrating a significant advantage in terms of the regulation in carrier dynamics even at ultra-low temperature. Interestingly, when the environmental temperature recovers from 10 K to RT, the photo-generated current for CsFAMA/FGCs device almost returns to the value before cooling, while huge loss is observed for those of the control devices, highlighting the important roles of embedded FGCs on the interfacial modification of PSCs.

To further verify the roles of embedding FGCs for enhanced photovoltaic performance of PSCs, FGCs were embedded in a similar manner into an FAPbI$_3$ perovskite layer (Supplementary **Fig. 21**)[37,38] to construct the FAPbI$_3$/FGCs based PSCs. As shown in **Fig. 4a** and **Table 1**, the FAPbI$_3$ device yields a champion PCE of 22.25%

measured in reverse scan, with V_{OC} of 1.102 V, J_{SC} of 25.30 mA/cm^{-2}, and FF of 79.81%. Notably, after the embedding of FGCs, the PCE is boosted to 24.02% with a large V_{OC} of 1.139 V and a remarkable FF of 82.21%. **Figure 4b** shows the corresponding EQE spectra of the champion devices with an integrated current density of 24.36 mA/cm^2 for pristine FAPbI$_3$ and 24.97 mA/cm^2 for FAPbI$_3$/FGCs, respectively, which agrees well with the *J-V* results. It is important to note that the reproducibility for all the devices is evaluated by collecting over 30 different batches, and the average PCE is improved from pristine 20.87 to 23.02% (**Fig. 4c**).

Pure α-FAPbI$_3$ is ideal for single junction solar cell due to its low band gap, as well as superior chemical and thermal stability[39], however its spontaneous conversion into the yellow non-perovskite phase (δ-FAPbI$_3$) under ambient conditions poses a serious challenge for practical applications. Results of environmental trials revealed that embedding FGCs in FAPbI$_3$ perovskite film significantly stabilize its α phase. As shown in **Fig. 4d**, the moisture stability for the FAPbI$_3$-based devices was conducted in a controlled temperature and humidity chamber (where temperature was set at 25 °C and humidity varied from 40% to 95%). At the initial stage (about 90 h) of RH=40%, the pristine FAPbI$_3$ device was found completely degraded, while the FAPbI$_3$/FGCs device could maintain its initial efficiency (23.45%). The FAPbI$_3$/FGCs device slowly degrades to 82% at the intermediate stage (60 h) of RH=40-95%, while maintaining ~60% of its initial PCE after 200 hours, even at the extreme stage of RH=95%, further verifying the important roles of FGC embedding on preventing moisture-induced perovskite degradation (Supplementary **Fig. 22**). The operational stability of FAPbI$_3$-based devices was also compared by MPP tracking at 60 °C under 1 sun illumination in **Fig. 4e.** After 500 h of exposure, the pristine FAPbI$_3$ device degrades to 58% of its initial PCE (21.97 %) whereas the target device maintained 89% of its initial PCE (23.02%), indicating boosted light & heat stability for PSCs embedded with FGCs.

Unravelling the roles of FGCs on interfacial engineering of PSCs. It has been reported that irreversible degradation of the ionic-type perovskite would be initiated due to gold diffusion and migration, as well as interaction

between gold and perovskite[36]. Strategies of embedding metal-based nanostructures with protective coatings into the perovskite layer have thus been developed to avoid the direct contact between metal and perovskite [28,40-42]. This work shows that the grafting of PFDT on gold enables the insulation of the contact between gold and perovskite, while differs apparently from the cases of utilizing the SPR effects of gold structures, which can be reflected from the truth that embedding of FGCs had little effect on the optical properties of the perovskite/FGCs films (Supplementary **Fig. 23**). It would thus be of interests to explore the roles of FGCs on the interfacial modification of PSCs, considering that the FGCs present more molecular features due to the dramatically decreased sizes, evidenced by the disappeared SPR absorption and emerged photoluminescence.

Ultraviolet photoelectron spectroscopy (UPS, **Fig. 5a**) measurements were used to investigate the detailed molecular structures of the FGCs, e.g. the highest occupied molecular orbital (HOMO) and the lowest unoccupied molecular orbital (LUMO) levels. Based on the optical bandgap (3.10 eV) (inset in **Fig. 5a**), Fermi energy level (16.12 eV), and the HOMO onset (0.99 eV) of FGC, the HOMO and LUMO values are calculated to be -6.09 eV and -2.89 eV, respectively, which identifies the molecular FGCs as p-type semiconductor feature. As shown in **Fig. 5b**, the Mott-Schottky (M-S) plots of the perovskite films with or without GNs embedding are determined as n-type semiconductor feature, while the perovskite film with the embedding of FGCs presents an inverted "V-shape" indicating the typical p-n junction feature that is similar with the reported literatures[43], further verifying the p-type semiconductor characteristic of the FGCs. The current-voltage (*I-V*) curves **(Fig. 5c)** show the roles of embedding the p-type FGCs on altering the electronic properties of the perovskite layers. It can be observed that the perovskite/FGCs films deposited on glass substrates[34,44] exhibit better conductivity than control films, suggesting that FGCs facilitate charge transfer between the adjacent grains. This can also be confirmed by the conducting atomic force microscopy (c-AFM, Supplementary **Fig. 24**)[44], where the dark current measured both at surface and GBs of the $FAPbI_3$/FGCs film is significantly higher than that of the $FAPbI_3$ film; it is proposed that this is a result

of the formed bulk p-n junction from the FGCs embedding. In addition, the misaligned logarithmic plots of the

control film under contrast sweep direction indicate the existence of ionic migration[34], whereas the perovskite/FGCs

film show almost coincident curves, owing to the anchoring effect formed by the strong hydrogen bonding between

fluorine groups in FGC and hydrogen atoms in organic cations of perovskite; further evidenced by analysis of the

Fourier-transform infrared spectroscopy (FTIR) and density functional theory (DFT) calculation (Supplementary

Note 2 and **Figs. 25-26**)[19].

The technique of time-resolved optical pump and terahertz (THz) probe (OPTP) was employed to further

investigate the carrier dynamics in the perovskite films upon the embedding of the FGCs. $FAPbI_3$ perovskite films

with or without FGCs embedding were deposited on z-cut quartz substrates, and then photoexcited with an 800 nm

(1.55 eV) optical pump beam (pump fluence of 600 $\mu J/cm^2$). The free carrier excitation and relaxation process of

$FAPbI_3$ and $FAPbI_3$/FGCs films on picosecond time scale were characterized by the ultrafast THz transmittance

changes ($\Delta T/T_0$), as shown in **Fig. 5d**. Striking differences of relative THz change in the decay dynamics can be

observed between films of $FAPbI_3$ and $FAPbI_3$/FGCs. To understand the relaxation dynamics of photoexcited free

carriers, the time-resolved $\Delta T/T_0$ was fitted by using biexponential decay functions $\Delta T/T_0 = [A_1\exp(-t/\tau_1) +$

$A_2\exp(-t/\tau_2)]$, where τ_1 and τ_2 represents the time constants for the fast and slow process, respectively[45]. The fitted

results (Supplementary **Fig. 27**) reveal that the fast process assisted by electron-phonon scattering is almost identical

(~13ps) regardless of the embedding of FGC, while the slow process exhibits slower relaxation (312ps) for the

$FAPbI_3$/FGC film than that of the $FAPbI_3$ film (256ps)[45]. The slower free carrier relaxation in $FAPbI_3$/FGC films is

considered related to the decreased recombination induced by trap states at GBs (Supplementary **Fig. 28**), attributed

to the $FAPbI_3$/FGC bulk heterojunction that provide an efficient separation channel for the photogenerated elctrons

and holes. Furthermore, the photoinduced attenuation in peak amplitude of THz pulse ($\Delta T/T_0$) is 25.5% in the

$FAPbI_3$/FGCs films at pump delay time of 5ps, which is higher than that observed (19.8%) in the $FAPbI_3$ films (see

inset in **Fig. 5d**). In general, the photoinduced $\Delta T/T_0$ are directly proportional to the real part of the photoconductivity[46], which reveals the in-phase motion of free electrons with the THz electric fields. To illustrate the change of real part of THz photoconductivity, the time-domain terahertz spectrum through films with no pump (blue solid line) and the photoinduced THz electric field change $\Delta E(t)$ were carried out based on the OPTP system. **Figure 5e** shows the photoinduced change in THz pulse $\Delta E(t)$ of FAPbI$_3$ and FAPbI$_3$/FGCs films at different pump delay time of 5ps, 13.6ps, 20ps, 53.6ps, respectively. The intensity of THz electric field through FAPbI$_3$ and FAPbI$_3$/FGCs films is at the same level in case of no pump, while the time-resolved $\Delta E(t)$ in FAPbI$_3$/FGC films is significantly higher than that of FAPbI$_3$ films.

The transient complex THz photoconductivity $\Delta\tilde{\sigma}(\tau)$ of FAPbI$_3$ and FAPbI$_3$/FGC films can be extracted at several times during free carrier relaxation dynamical process, allowing for further investigation. Based on the THz transmission line model, the transient change of complex THz photoconductivity $\Delta\tilde{\sigma}(\tau)$ is calculated using the equation[47]:

$$\Delta\tilde{\sigma}(\tau) = \frac{(n_{Air} + n_{Sub})}{T_0 d z_0} \Delta T(\tau) \ ,$$

where $\Delta T(\tau)$ is the change in frequency-domain THz transmission at pump delay time of τ ps and T_0 is the frequency-domain THz transmission through film at no optical pump, n_{air} and n_{sub} are the refractive index of air (equal to 1) and substrate (2.53), respecitively, d is the thickness of the perovskite films (500 nm) and Z_0 is the impedance of free space (377Ω)[48].

The real ($\Delta\sigma_{real}$) THz photoconductivity spectra of FAPbI$_3$ and FAPbI$_3$/FGCs films at 5ps pump-probe delays are shown in **Fig. 5f**. The clear enhancement of real ($\Delta\sigma_{real}$) THz photoconductivity as can be observed in FAPbI$_3$/FGC film in contrast to that of FAPbI$_3$ films. The change of THz photoconductivity is related to the photogenerated carrier density and the mobility of the free carriers[49]. It is proposed that the FAPbI$_3$ films with or without embedding of FGCs in this study have the same photoinduced carrier density when photoexciting at 800 nm, owing to the optically

inactive FGC (wide band-gap of 3.1 eV) under such photon energy of the pump beam. The enhancement in $\Delta\sigma_{real}$ thus indicates the improvement of carrier mobility in the FAPbI$_3$/FGCs films, further evidenced by the results of the space-charge-limited-current (SCLC, Supplementary **Fig. 28**)[20].

A conclusion from the OPTP analysis is that carrier dynamics were effectively modulated when perovskite films were embedded with FGCs due to the formed heterojunction between FAPbI$_3$ and FGC, as shown schematically in **Fig. 5g**. This provides an extra channel at GBs to favor carrier separation and facilitate the photogenerated holes transfer along the FGC at GBs and collection by hole-transport layer (HTL). Regarding the FGCs located at the interface between perovskite and HTL, further investigation of the interfacial carrier transfer process was performed by applying the M-S relation (Supplementary **Fig. 29**)[34,44], which indicates that the perovskite/FGCs devices have less charge accumulation at the interface between perovskite and Spiro-OMeTAD. This is attributed to the optimized interface band-alignment induced by FGCs, where the lower valence band maximum of the perovskite/FGC film effectively decreases the interface barrier (**Fig. 5h**), evidenced by the analyses of UPS spectra (Supplementary **Fig. 30**).

Discussion

Even though the technique of laser irradiation in liquid has the advantage of generating nanocrystals in desired solvents, the adopting of FGCs in this work was based on the systematical selection of the solvents and ligands (Supplementary **Note 1**), which provides a series of additives to be screened for optimized interfacial embedding. The ligand of PFDT were also found helpful for improved efficiency of PSCs owing to the passivation groups of -SH[50] which, however, failed to provide performance as good as the case of FGCs (Supplementary **Fig. 31**). It is proposed that this is due to the unique role of the bifunctional mediator the FGCs perform, especially with respect to the carriers dynamics modulation. It should be noted that the PFDT could be effectively utilized to graft on the FGCs through controlling the laser irradiation time and regulating the concentration of the PFDT in EA

(Supplementary **Fig. 14** and **Note 1**), which thus exclude the influence of PFDT on efficiency enhancement of PSCs upon FGCs embedding. In addition, the ligand of PFDT used in this work has three functions: (i) unique size-reducing function that enables the metal-semiconductor transfer of the laser generated gold nanocrystals, allowing for the formation of the bulk heterojuction for enhanced charge separation; (ii) forming firm Au-S covalent bonding that could anchor the Au and insulate the contact between Au and perovskite to restrain ionic-type perovskite from irreversible degradation upon the gold diffusion and migration; (iii) the hydrophobic tails of PFDT prevents the moisture degradation of the perovskite and the fluorine groups could form hydrogen bonding with perovskite that inhibits the ionic migration and favors for thermal and operational stability.

The laser manufactured FGCs with molecular-like behavior, along with the surface fluorination, play unique roles as effective interfacial mediators in terms of the advantages on carrier dynamics by reducing the carrier recombination and boosting the charge extraction. They also increase environmental stability through inhibiting moisture invasion and suppressing ionic migration, leading to the significant improvement of PSCs performances. By merits of these efficient interfacial mediating factors, a champion PCE up to 24.02% with significantly enhanced environmental stability based on the FAPbI$_3$ solar cells was achieved. The importance that the PSCs based on the mixed-cation perovskite can deliver more than 10000 hours of moisture stability is highlighted due to this being one of the main challenges preventing commercialization; in particular, with regards to the FAPbI$_3$, the significantly enhanced phase stability under high RH demonstrates excellent moisture stability. According to current available records, the resulted efficiency and moisture stability of CsFAMA- and FAPbI$_3$-based perovskites rank among the top records in PSCs decorated with nanocrystals based additives (Supplementary **Table 1**). In addition, under thermal and/or operational condition, the major factors causing the degradation of the perovskite devices are attributed to the highly mobile ions in perovskite films[51]. Embedding FGCs in perovskite films enables the suppression of ionic migration and phase separation (**Fig. 5c** and Supplementary **Fig. 32**), resulting in significantly

improved thermal and operational stability. The interfacial embedding of the additives with the bi-function of improving the charge transfer/extraction and environmental stability is thus highly promising to advance the development of highly efficient and stable PSCs.

In summary, we have demonstrated an efficient strategy of addressing the interfacial loss of PSCs through interfacial embedding of laser manufactured gold clusters with p-type semiconducting feature in the layer of the perovskite. The formed Au-S covalent bonding in FGCs firmly anchored the Au core and insulated the contact between Au and perovskite, avoiding the general irreversible degradation of the ionic-type perovskite upon the gold diffusion and migration. The hydrophobic tails of PFDT and hydrogen bonding formed between fluorine groups and perovskite greatly enhanced the PSCs stability and resistance to degradation from moisture, thermal and light. The p-type semiconducting feature enables the FGCs efficient interfacial mediator to improve the carrier dynamics by boosting the charge extraction at grain boundaries and reducing the interfacial carrier transfer, evidenced by the OPTP analysis and Mott-Schottky plots. Benefiting has resulted in the creation of highly efficient FAPbI$_3$ solar cells with a champion PCE up to 24.02% and significantly enhanced phase stability under high RH, as well as highly efficient CsFAMA based PSCs with moisture stability (RH of 75%) over 10000 hours being successful. It is believed that this study will be inspiring to further work manipulating the physical/chemical features of perovskite films via embedding bi-functional interfacial mediators for advanced photovoltaics based on laser-matter interactions.

Methods

Materials. Unless stated otherwise, all materials were purchased from Sigma-Aldrich and used as received. Fuorine-doped tin oxide (FTO) glass substrates were obtained from Pilkington. Spiro-OMeTAD (2,2',7,7'-Tetrakis[N,N-di(4-methoxyphenyl)amino]-9, 9'-spirobifuorene, ≥99.8% purity), 4-tert-butylpyridine (tBP, ≥99.9% purity) and lithium-bis (trifluoromethanesulfonyl) imide (Li-TFSI, ≥99.9% purity) were supplied by Xi'an Polymer Light Technology Corp. Bulk gold was obtained from Zhongnuo Advanced Material (Beijing) Co., Ltd. China.

Preparation of the GN and FGC. A bulk gold plate was placed in a reaction cell with 5 ml ethyl acetate for irradiation. An Nd:YAG non-focusing pulsed laser (repetition rate: 10 Hz, pulse width: 8 ns, beam diameter: 8 mm) with a wavelength of 355 nm was used to irradiate the gold in ethyl acetate with or without the presence of PFDT in an inert environment. During irradiation, a magnetic stirrer was used to keep the solution homogeneous. The laser fluence varied from 0-700 mJ/pulse cm^{-2}.

Device fabrication. The FTO substrate was cleaned with successive sonication in detergent, ultrapure water, acetone and ethanol for 20 min, respectively, and then dried under N_2 flow and treated by ozone plasma for 15 min to remove the organic residual and enhance the wettability. A ~50 nm thick TiO_2 compact layer was prepared by chemical bath deposition. The spin-coating was accomplished in a nitrogen glovebox. For the preparation of mixed-cation perovskite, a 1.2 M "mixed" perovskite precursor solution containing CsI (0.06 M), FAI (0.97 M), PbI_2 (0.97 M), MABr (0.17 M) and $PbBr_2$ (0.17 M), was stirred in a mixture of DMF and DMSO (4:1 v/v) at 60 °C for 2 h. The resulting solution was coated onto the FTO/TiO_2 substrate by a consecutive two-step spin-coating process at 1,000 and 4,000 r.p.m for 10 and 30 s, respectively. During the second step, 200 μl anti-solvent or GNs/FGCs colloid solution was immediately poured on the spinning substrate 10 s prior to the end of the program. Thereafter, the substrate was put onto a hotplate for 60 min at 100 °C, forming the $Cs_{0.05}FA_{0.81}MA_{0.14}PbI_{2.55}Br_{0.45}$ film. $FAPbI_3$ perovskite precursor solution is prepared by dissolving a mixture of PbI_2 (783.8 mg), FAI (292.4 mg) and MACl (45.8 mg) in 1 ml mixed solution of DMF and DMSO (4:1 v/v) at ~60 °C to assist dissolving. $FAPbI_3$ solution was coated onto the FTO/TiO_2 substrate by a single step spin-coating process at 5,000 r.p.m for 60 s. 200 μl anti-solvent or GNs/FGCs colloid solution was immediately poured on the spinning substrate 20 s prior to the end of the program. After spin-coating, the substrate was put onto a hotplate for 10 min at 150 °C, forming the $FAPbI_3$ film. After the deposition of perovskite films, a HTM solution was then deposited by spin coating at 5,000 r.p.m. for 30 s. The Spiro-OMeTAD solution was prepared by dissolving 72.3 mg Spiro-OMeTAD, 28.8 μL tBP and 17.5 μL of a stock solution of 520 mg/mL Li-TFSI in acetonitrile in 1 mL chlorobenzene. Finally, an 80 nm thick Au electrode was deposited by thermal evaporation. The active area of this electrode was 0.1 cm^2, which was calculated by a mask plate and further determined by an optical microscope.

Characterizations and measurements. Simulated AM 1.5G irradiation (100 mW cm^{-2}) was produced by a xenon-lamp-based solar simulator (Oriel 67005, 150 W Solar Simulator) for *J-V* measurements. The light intensity was calibrated by a silicon (Si) diode (Hamamatsu S1133) equipped with a Schott visible-color glass filter (KG5 color-filter). A Keithley 2420 Source-Meter was used for *J-V* measurement with a scanning rate of 0.1V/s. External quantum efficiencies were characterized with a Newport QE measurement kit by focusing a monochromatic beam of light onto the devices. For the steady-state output measurement, the solar cells were put under the simulated AM 1.5G, 1-sun illumination to record the photocurrent under a bias voltage. The morphology and structure of the samples were characterized by a field emission SEM (FEI Verios G4). c-AFM measurements were performed on an Asylum Research MFP-3D-Origin AFM using Au-coated Si conductive probes (HA_HR, NT-MDT). TEM was performed by using an FEI Talos F200X equipped with a field emission gun (FEG) operated at 200 kV. X-ray diffraction (XRD) spectra were recorded on a PANAlyticalX'pert PRO equipped with a diffracted beam monochromator, and a conventional cobalt target X-ray tube set to 40 kV and 30 mA. X-ray photoelectron

spectroscopy (XPS) measurements were conducted on an Axis Supra (Kratos). The Valance band (VB) spectra were measured with a monochromatic He I light source (21.22 eV) and a VG Scienta R4000 analyzer. The absorption was measured using the ultraviolet-visible (Uv-vis) spectrophotometer (Perkin-Elmer Lambda 35 UV-vis-NIR). The M-S measurements of the perovskite films and its devices were carried out by a electrochemical workstation (CHI660E).

Time-resolved Optical Pump Terahertz Probe spectroscopy

The time-resolved Optical Pump Terahertz Probe spectroscopy (OPTPS) was employed to explore the photoinduced ultrafast dynamics of perovskites by 800 nm femtosecond laser. Here, a pulse energy of 8-mJ, pulse width of 40-fs femtosecond laser at 800 nm with 1 kHz repetition rate was used in OPTPS system and the laser pulse was divided into three beams: the first part and second part were used to generate THz and detect the THz wave, which forms a THz-TDS system. The third part of laser as optical pump was used to photoexcite the sample. In this experiment, the area of the optical pump spot was about 0.4 cm^2, which is larger than the area of the focused THz beam (diameter is 3 mm) to ensures the homogeneous photoexcitation. The transmissive THz pulse through sample with no pump and substrate were probed based on the part of THz-TDS system. Furthermore, the peak of THz pulse was fixed by the delay line and the dynamic processes of THz transmittance change ($\triangle T/T_0$) of sample photoexcited were traced by controlling another delay line. In order to reveal the ultrafast photoinduced free charge carriers, frequency-resolved complex THz spectra at each pump-probe delay were monitored by scanning the THz pulse at fixed pump delay point. The change of THz photoconductivity in different photoexcitation decay dynamics were calculated from the THz transmittance change ($\triangle T/T_0$).

Stability test. Moisture-stability measurements of the non-encapsulated films/solar cells were performed in a constant temperature & humidity incubator in dark. PCEs of the devices were periodically measured under AM1.5 G simulated sun light in ambient air. Thermal-stability of the non-encapsulated solar cell was tested on a hot plate (85 °C) in a nitrogen atmosphere. PCEs of the devices were periodically measured under AM1.5 G simulated sun light after cooling the devices down to room temperature. Long-term operational stability of the non-encapsulated devices were measured under AM1.5 G simulated sun light in a nitrogen atmosphere.

Data availability

The authors declare that the data supporting the findings of this study are available within the article and its Supplementary Information files.

References

[1]   Best Research-Cell Efficiency Chart (NREL, 2020); https://www.nrel.gov/pv/assets/pdfs/pv-efficiency-chart.20200925.pdf

[2]   Gao, L. et al. Efficient near-infrared light-emitting diodes based on quantum dots in layered perovskite. *Nat. Photonics*. **14,** 227-233 (2020).

[3]   Zhao, J. et al. Perovskite-filled membranes for flexible and large-area direct-conversion X-ray detector arrays. *Nat. Photonics*. **14,** 612-617 (2020).

[4]   Jian, J. et al. Embedding laser generated nanocrystals in BiVO4 photoanode for efficient photoelectrochemical water splitting. *Nat. Commun.* **10,** 2609 (2019).

[5]   Hou, Y. et al. A generic interface to reduce the efficiency-stability-cost gap of perovskite solar cells. *Science*, **358,** 1192-1197 (2017).

[6]   Wang, Y. et al. Stabilizing heterostructures of soft perovskite semiconductors. *Science*, **365,** 687-691 (2019).

[7]   Yang, S. et al. Stabilizing halide perovskite surfaces for solar cell operation with wide-bandgap lead oxysalts. *Science*, **365,** 473-478 (2019).

[8]   Ono, L. K., Liu, S. & Qi, Y. Reducing detrimental defects for high-performance metal halide perovskite solar cells. *Angew. Chem. Int. Ed.* **59,** 6676-6698 (2020).

[9]   Ran, C., Xu, J., Gao, W., Huang, C. & Dou, S. Defects in metal triiodide perovskite materials towards high-performance solar cells: origin, impact, characterization, and engineering. *Chem. Soc. Rev.* **47,** 4581-4610 (2018).

[10]   Li, N. et al. Microscopic Degradation in Formamidinium-Cesium Lead Iodide Perovskite Solar Cells under Operational Stressors. *Joule* **4,** 1743-1758 (2020).

[11]   Wang, Q. et al. Scaling behavior of moisture-induced grain degradation in polycrystalline hybrid perovskite thin films. *Energy Environ. Sci.* **10,** 516-522 (2017).

[12]   Aristidou, N. et al. Fast oxygen diffusion and iodide defects mediate oxygen-induced degradation of perovskite solar cells. *Nat. Commun.* **8,** 15218 (2017).

[13]   Rong, Y. et al. Challenges for commercializing perovskite solar cells. *Science* **361,** eaat8235 (2018).

[14]   Guo, P. et al. Surface & grain boundary co-passivation by fluorocarbon based bifunctional molecules for perovskite solar cells with efficiency over 21%. *J. Mater. Chem. A* **7,** 2497-2506 (2019).

[15]   Guo, P. et al. Double barriers for moisture degradation: assembly of hydrolysable hydrophobic molecules for stable perovskite solar cells with high open-circuit voltage. *Adv. Funct. Mater.* **30,** 2002639 (2020).

[16]   Wang, R. et al. Constructive molecular configurations for surface-defect passivation of perovskite photovoltaics. *Science* **366,** 1509-1513 (2019).

[17]   Zheng, X. et al. Managing grains and interfaces via ligand anchoring enables 22.3%-efficiency inverted perovskite solar cells. *Nat. Energy* **5,** 131-140 (2019).

[18]   Zong, Y. et al. Continuous grain-boundary functionalization for high-effifficiency perovskite solar cells with exceptional stability. *Chem* **4,** 1404-1405 (2018).

[19]   Yang, J. et al. High-performance perovskite solar cells with excellent humidity and thermo-stability via fluorinated perylenediimide. *Adv. Energy Mater.* **9,** 1900198 (2019).

[20]   Guo, P. et al. Laser-generated nanocrystals in perovskite: universal embedding of ligand-free and sub-10 nm nanocrystals in solution-processed metal halide perovskite films for effectively modulated optoelectronic performance. *Adv. Energy Mater.* **9,** 1901341 (2019).

[21]   Hsu, H.-H. et al. Carbon nanodot additives realize high-performance air-stable p-i-n perovskite solar cells providing efficiencies of up to 20.2%. *Adv. Energy Mater.* **9,** 1901341 (2019).

[22]   Gong, X. et al. Black phosphorus quantum dots in inorganic perovskite thin films foreffieient photovoltaic application. *Sci. Adv.* **6,** eaay5661 (2020).

[23]   Hosokawa, H. et al. Solution-processed intermediate-band solar cells with lead sulfide quantum dots and lead halide perovskites. *Nat. Commun.* **10,** 43 (2019).

[24]   Liu, M. et al. Lattice anchoring stabilizes solution-processed semiconductors. *Nature* **570,** 96-101 (2019).

[25]   Chen, X. et al. Dual interfacial modification engineering with 2D MXene quantum dots and copper sulphide nanocrystals enabled high-performance perovskite solar cells. *Adv. Funct. Mater.* **30,** 2003295 (2020).

[26]   Agresti, A. et al. Titanium-carbide MXenes for work function and interface engineering in perovskite solar cells. *Nat. Mater.* **18,** 1228-1234 (2019).

[27]   Yu, H. et al. Laser generated supranano liquid metal as efficient electron mediator in hybrid perovskite solar cells. *Adv. Mater.* **32,** 202001571 (2020).

[28]   Qin, P. et al. Grain boundary and interface passivation with core-shell Au@CdS nanospheres for high-efficiency perovskite solar cells. *Adv. Funct. Mater.* **30,** 1908408 (2020).

[29]   Jin, R., Zeng, C., Zhou, M. & Chen, Y. Atomically precise colloidal metal nanoclusters and nanoparticles: fundamentals and opportunities. *Chem. Rev.* **116,** 10346-10413 (2016).

[30]   Jin, R. Quantum sized, thiolate-protected gold nanoclusters. *Nanoscale* **2,** 343-362 (2010).

[31]   Zhang, J. et al. Microwave-facilitated rapid synthesis of gold nanoclusters with tunable optical property for sensing ions and fluorescent ink. *Chem. Commun.* **51,** 10539-10542 (2015).

[32]   Vogt, A. D. et al. Adsorption of 11-mercaptoundecanoic acid on Ni(111) and its interaction with probe molecules. Langmuir **13,** 3397-3403 (1997).

[33]   Tang, Z., Xu, B., Wu, B., Germann, M. W. & Wang, G. Synthesis and structural determination of multidentate 2,3-dithiol-stabilized Au clusters. *J. Am. Chem. Soc.* **132,** 3367 (2010).

[34]   Bu, T. et al. Universal passivation strategy to slot-die printed SnO_2 for hysteresis-free efficient flexible perovskite solar module. *Nat. Commun.* **9,** 4609 (2018).

[35]   Li, H. et al. Graphdiyne-based bulk heterojunction for efficient and moisture-stable planar perovskite solar cells. *Adv. Energy Mater.* **8,** 1802012 (2018).

[36]   Domanski, K. et al. Not all that glitters is gold: metal-migration-induced degradation in perovskite solar cells. *ACS Nano* **10,** 6306-6314 (2016).

[37]   Min, H. et al. Efficient, stable solar cells by using inherent bandgap of a-phase formamidinium lead iodide. *Science* **366,** 749-753 (2019).

[38]   Kim, M. et al. Methylammonium chloride induces intermediate phase stabilization for efficient perovskite solar cells. *Joule* **3,** 2179-2172 (2019).

[39]   Liu, Y. et al. Stabilization of highly efficient and stable phase-pure $FAPbI_3$ perovskite solar cells by molecularly tailored 2D-overlayers. *Angew. Chem. Int. Ed.* **59,** 15688-15694 (2020).

[40]   Ghosh, A. et al. Core/shell nanocrystal tailored carrier dynamics in hysteresisless perovskite solar cells with ~20% Efficiency and long operational stability. *J. Phys. Chem. Lett.* **11,** 591-600 (2020).

[41]   Zhang, C. et al. Efficient perovskite solar cells by combination use of Au nanoparticles and insulating metal oxide. *Nanoscale* **9,** 2852-2864 (2017).

[42]   Ye, T. et al. Performance enhancement of tri-Cation and dual-anion mixed perovskite solar cells by Au@SiO2 nanoparticles. *Adv. Funct. Mater.* **27,** 1606545 (2017).

[43]   Zhang, J. & Zhang, L. Incorporation of CoO nanoparticles in 3D marigold flower-like hierarchical architecture $MnCo_2O_4$ for highly boosting solar light photo-oxidation and reduction ability. *Appl. Catal. B: Environ.* **237,** 1-8 (2018).

[44]   Wu, W.-Q. et al. Molecular doping enabled scalable blading of efficient hole-transport-layer-free perovskite solar cells. *Nat. Commun.* **9,** 1625 (2018).

[45]   Kumar, A. et al. Excitons in 2D perovskites for ultrafast terahertz photonic devices. *Sci. Adv.* **6,** eaax8821 (2020).

[46]   He, C. et al. Competition between free carriers and excitons mediated by defects observed in layered WSe_2 crystal with time-resolved terahertz spectroscopy. *Adv. Opt. Mater.* **6,** 1800290 (2018).

[47]   Chanana, A., Liu, X., Zhang, C, Vardeny, Z. V. & Nahata, A. Ultrafast frequency-agile terahertz devices using methylammonium lead halide perovskites. *Sci. Adv.* **4,** eaar7353 (2018).

[48]   Yan, H. et al. Tunable infrared plasmonic devices using graphene/insulator stacks. *Nat. Nanotechnol.* **7,** 330-334 (2012).

[49]   Wehrenfennig, C., Eperon, G. E., Johnston, M. B., Snaith, H. J. & Herz, L. M. High charge carrier mobilities and lifetimes in organolead trihalide perovskites. *Adv. Mater.* **26,** 1584-1589 (2014).

[50]   Wu, Z. et al. Highly efficient perovskite solar Cells enabled by multiple ligand passivation. *Adv. Energy Mater*. **10,** 1903696 (2020).

[51]   Lee, J.-W. et al. 2D perovskite stabilized phase-pure formamidinium perovskite solar cells. *Nat. Commun.* **9,** 3021 (2018).

Acknowledgements

Author contributions

H.Q.W. and P. G. conceived the concept and designed the project. H.Z., L.Z and W.H. designed and performed the OPTPS experiment. Y.Q. and H.Y.W gave advice on the preparation of gold clusters. W.Z., N.J. and C.L. contributed to the fabrication of high performance PSCs. X.Z. designed and performed the DFT calculations. J.M.U. and A.H. carried out the alternating-temperature experiment. Q.Y., V.A.V., E.I. and D.S. analysed data and revised the manuscript. H.Q.W., P.G. and H.Zhu. wrote the paper. All authors discussed the results and commented on the paper. P.G. and H.Z. have contributed equally to this work.

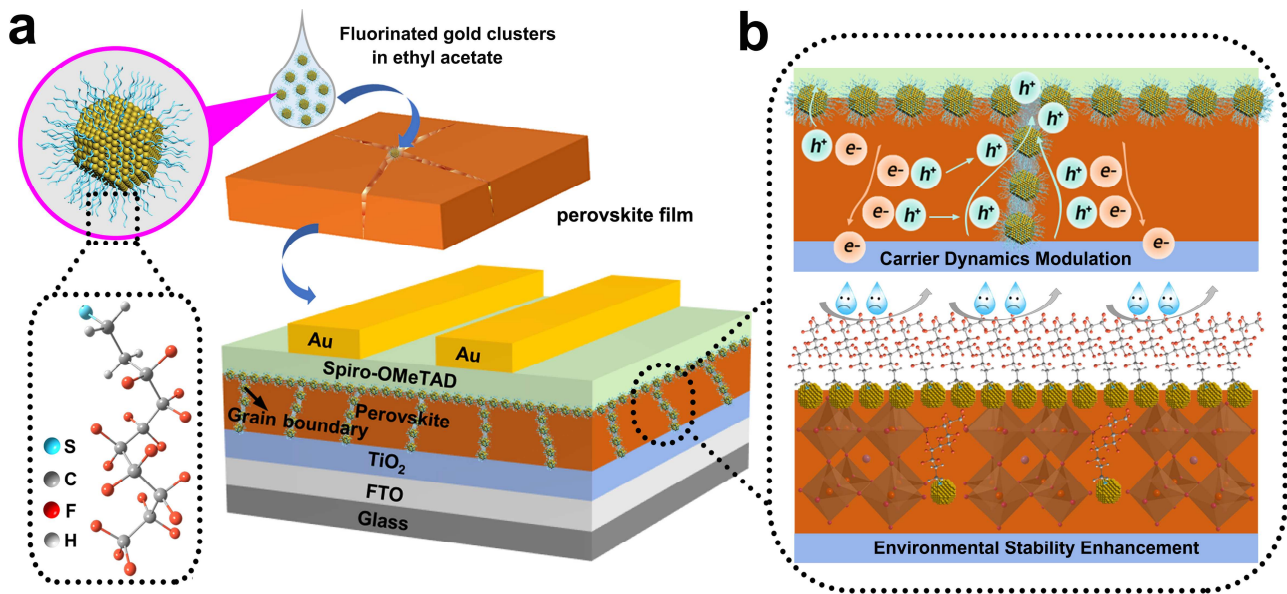# Competing interests

The authors declare no competing interests.

Figure 1 Laser manufactured hydrophobic FGCs as bifunctional interfacial mediator. a, Schematic illustration of interfacial embedding FGCs in the layer of perovskite. **b**, Schematic illustration of the function of FGCs for carrier dynamics modulation and improving environmental stability.
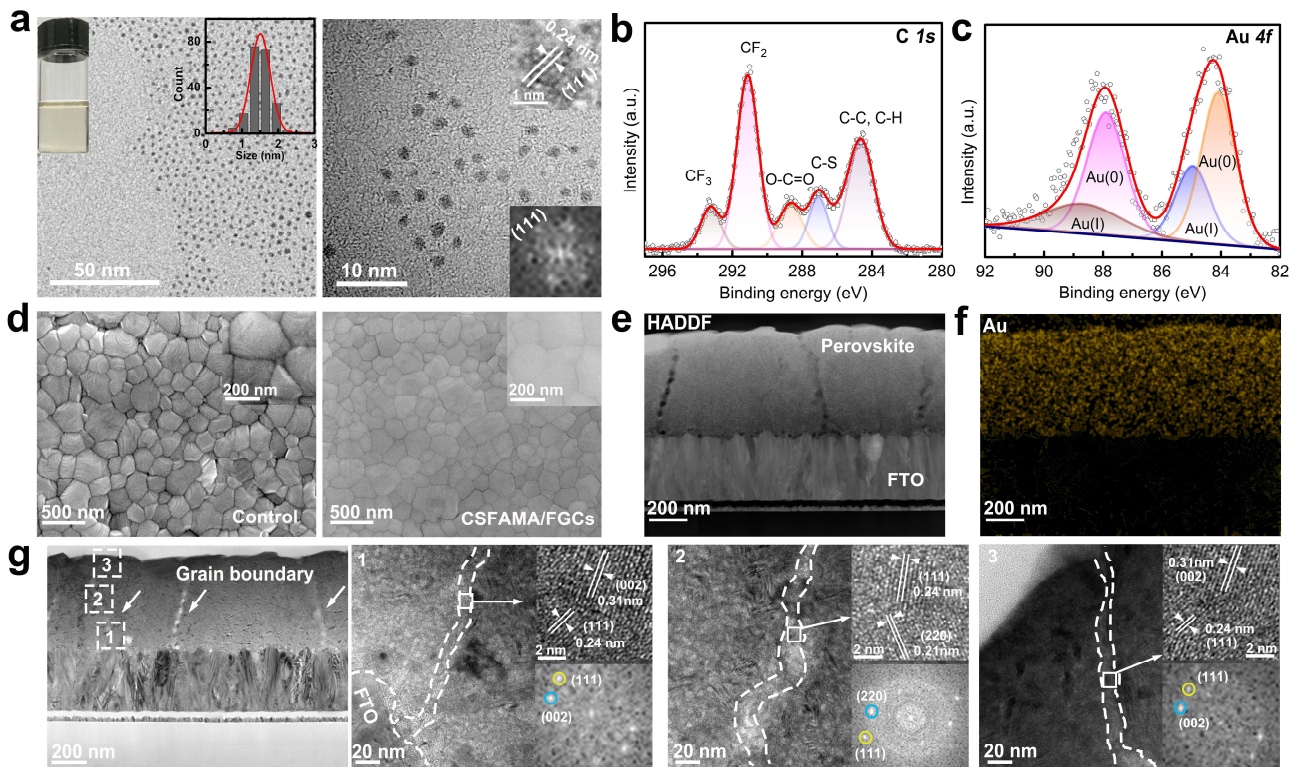
Figure 2 Interfacial embedding of FGCs into perovskite films. a, Low-magnified (left) and high-magnified (right) TEM images of FGCs. Insets in left of (**a**) are corresponding colloidal solution picture and size distribution histogram. Insets in right of (**a**) are corresponding HRTEM and FFT images. **b,c**, High-resolution XPS spectra of C 1s and Au 4f for the FGCs. **d**, Top-view SEM images of the control (left) and CsFAMA/FGCs (right) films. **e,f**, Cross-sectional HADDF image and corresponding EDS image for the CsFAMA/FGCs film. **g**, Cross-sectional TEM image and corresponding HRTEM images and FFT patterns of the region in the dotted rectangle for the CsFAMA/FGCs film. Blue and yellow circles in FFT patterns represent the perovskite and gold phases, respectively.
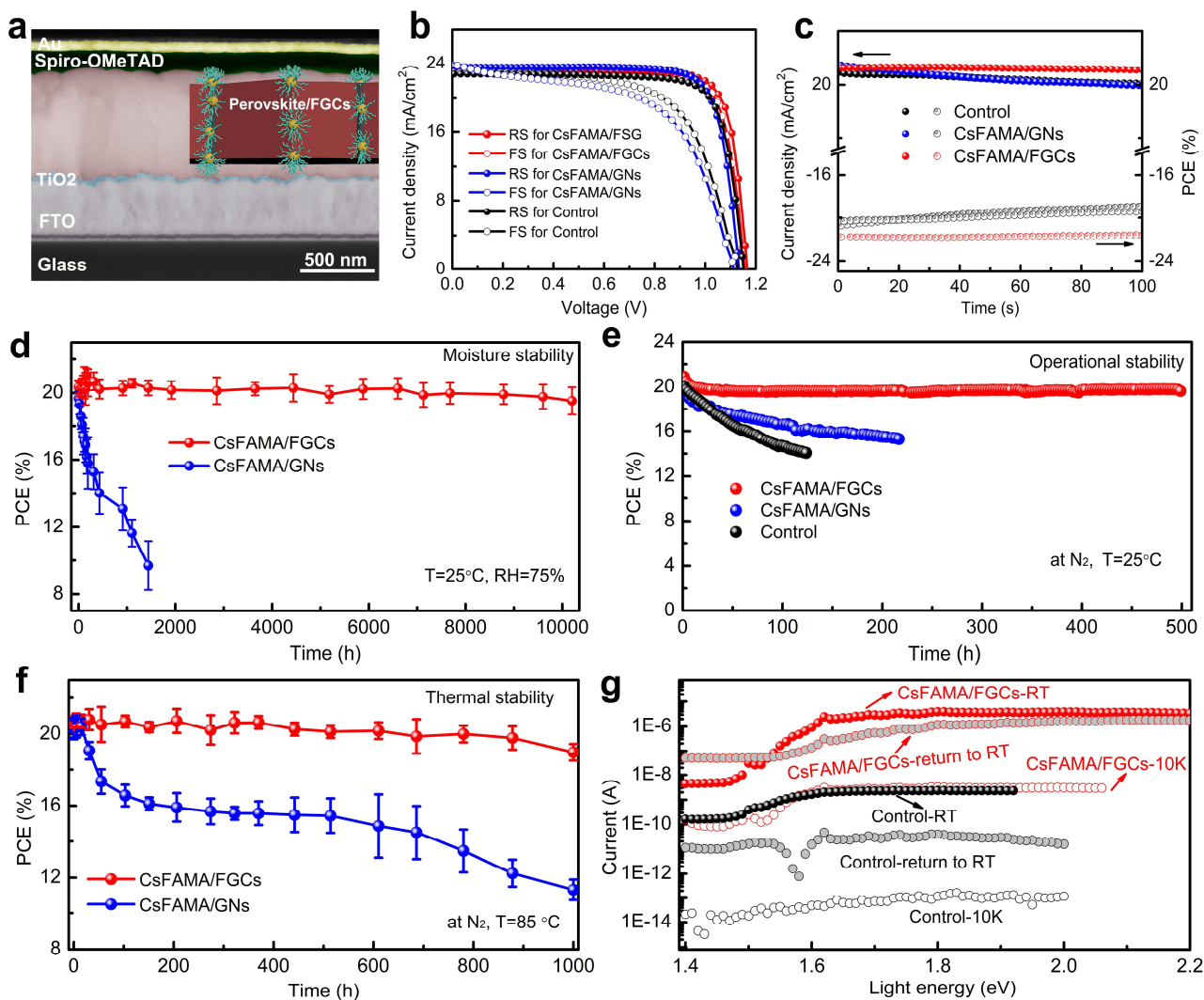
Figure 3 Photovoltaic performance of CsFAMA-based PSCs. All devices are unencapsulated. **a**, Cross-sectional SEM image of the CsFAMA/FGCs device. **b**, *J-V* curves measured by reverse and forward scans of the champion devices based on control, CsFAMA/GNs and CsFAMA/FGCs. **c**, Steady-state photocurrent and output PCE for control, CsFAMA/GNs and CsFAMA/FGCs devices at the maximum power point of 0.96 V, 0.94 V and 0.98 V, respectively. **d**, Moisture stability of the CsFAMA/GNs and CsFAMA/FGCs devices in relative humidity of 75%. **e**, Operational stability of the control, CsFAMA/GNs and CsFAMA/FGCs devices on continuous AM 1.5G illumination in an inert atmosphere. **f**, Thermal stability of the CsFAMA/GNs and CsFAMA/FGCs devices under heating stress (85°C) in an inert atmosphere. In (**d**) and (**f**), the error bars represent the standard deviation for 10 devices. **g**, Alternating temperature test for the control and CsFAMA/FGCs devices.
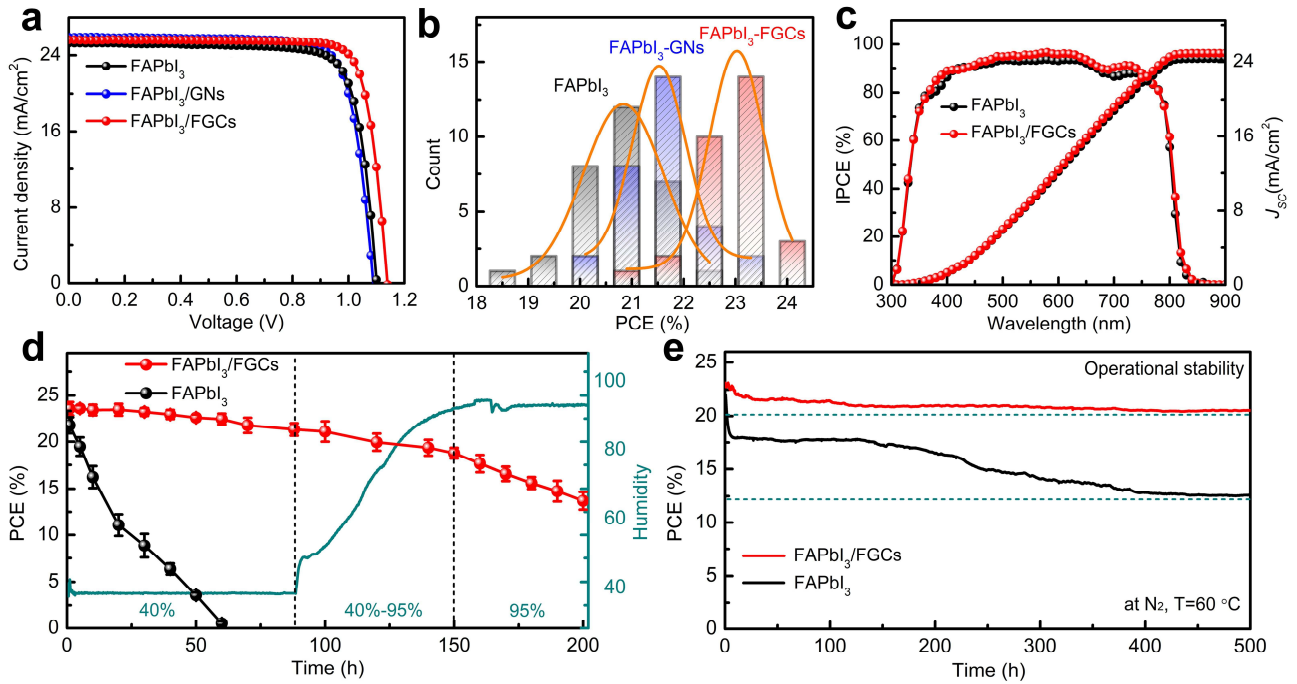
Figure 4 Photovoltaic performance of FAPbI₃-based PSCs. All devices are unencapsulated. **a**, *J-V* curves measured by reverse scan of the champion devices based on FAPbI$_3$, FAPbI$_3$/GNs and FAPbI$_3$/FGCs films. **b**, PCE distribution of FAPbI$_3$, FAPbI$_3$/GNs and FAPbI$_3$/FGCs devices. **c**, EQE and integrated current density curves of the champion devices for FAPbI$_3$ and FAPbI$_3$/FGCs devices. **d**, Moisture stability of the FAPbI$_3$ and FAPbI$_3$/FGCs devices in a variable humidity range. The error bars represent the standard deviation for 10 devices. **e**, Operational stability of the FAPbI$_3$ and FAPbI$_3$/FGCs devices under continuous AM 1.5G illumination at 60 °C in an inert atmosphere.
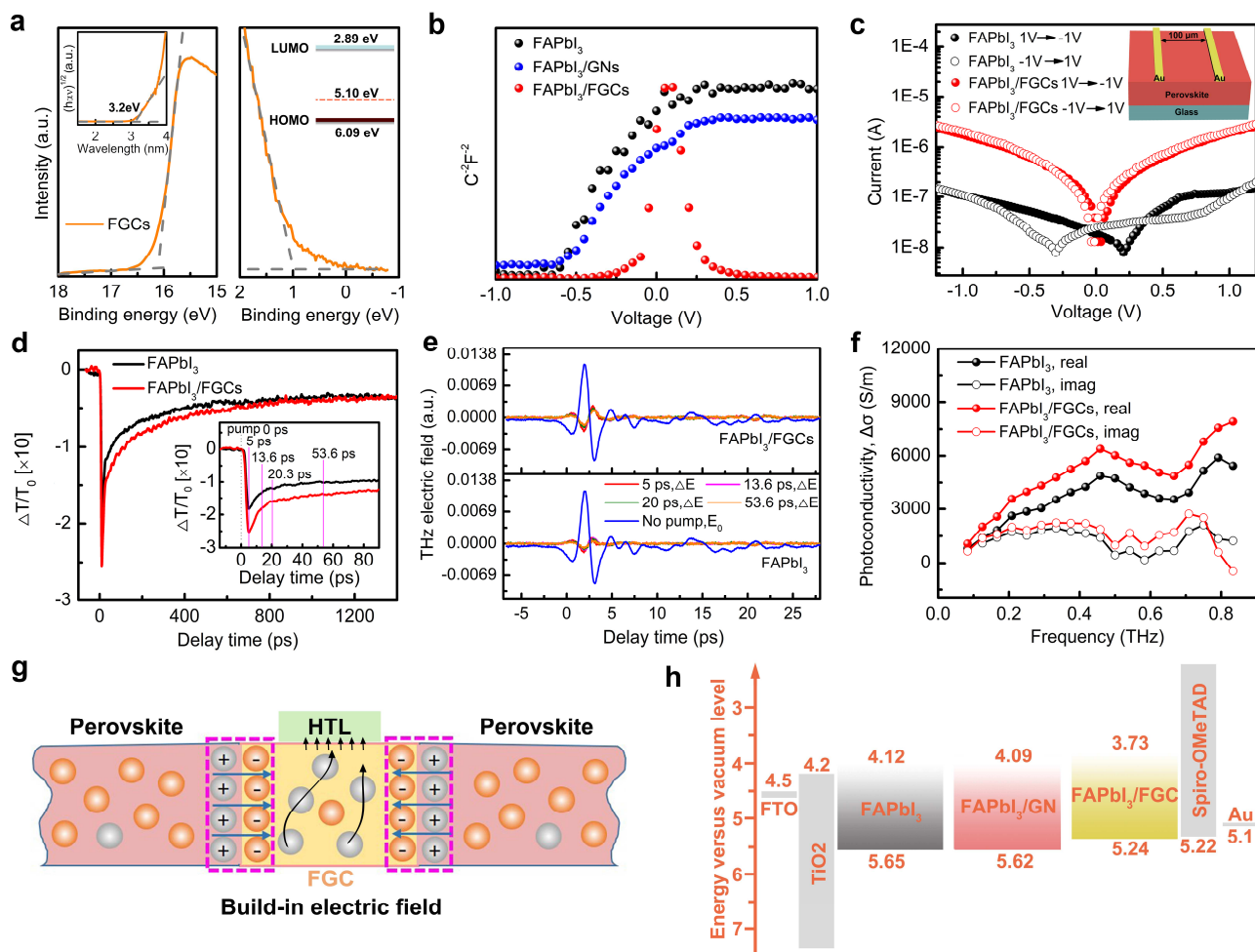
Figure 5 Roles of FGCs on interfacial engineering of PSCs. a, UPS spectra of FGCs. The insets show the bandgap and energy level diagram of FGCs. **b,** Mott-Schottky plots of the $FAPbI_3$, $FAPbI_3/GNs$, and $FAPbI_3/FGCs$ films, respectively. **c**, Logarithmic *I-V* plots of $FAPbI_3$ and $FAPbI_3/FGCs$ films. **d**, Free carrier excitation and relaxation dynamics of the $FAPbI_3$ and $FAPbI_3/FGCs$ films. The inset shows corresponding magnified curves. **e**, Time-domain terahertz pulses through the $FAPbI_3$ and $FAPbI_3/FGCs$ films at different pump delay time. **f**, Photoconductivity spectra of the $FAPbI_3$ and $FAPbI_3/FGCs$ films. **g**, Schematic diagram for the construction of the build-in electric field. **h**, Schematic diagrams of the band structure of the PSCs based on the $FAPbI_3$, $FAPbI_3/GNs$, and $FAPbI_3/FGCs$ films.

Table 1 Photovoltaic parameters (reverse scan) of the champion devices based on different perovskite films.

Sample	V_{oc} (V)	J_{sc} (mA/cm^2)	FF (%)	PCE (%)	Average (%)
CsFAMA	1.150	22.80	78.84	20.67	19.62
CsFAMA/GNs	1.133	23.58	79.95	21.36	20.01
CsFAMA/FGCs	1.166	23.12	81.23	21.90	21.02
FAPbI$_3$	1.102	25.30	79.81	22.25	20.87
FAPbI$_3$/GNs	1.087	25.92	80.88	22.79	21.53
FAPbI$_3$/FGCs	1.139	25.65	82.21	24.02	23.02